The Boreal Winter El Niño Precipitation Response over North America: Insights into Why January Is More Difficult to Predict Than February

YOUNG-KWON LIM

Global Modeling and Assimilation Office, NASA Goddard Space Flight Center, Greenbelt, and Goddard Earth Sciences Technology and Research/Universities Space Research Association, Columbia, Maryland

SIEGFRIED D. SCHUBERT

Global Modeling and Assimilation Office, NASA Goddard Space Flight Center, Greenbelt, and Science Systems and Applications, Inc., Lanham, Maryland

YEHUI CHANG

Global Modeling and Assimilation Office, NASA Goddard Space Flight Center, Greenbelt, and Goddard Earth Sciences Technology and Research/Morgan State University, Baltimore, Maryland

HAILAN WANG

NOAA Climate Prediction Center, College Park, Maryland

(Manuscript received 12 November 2019, in final form 17 July 2020)

ABSTRACT

This study examines the within-season monthly variation of the El Niño response over North America during December–March using the NASA/GEOS model. In agreement with previous studies, the skill of 1-month-lead GEOS coupled model forecasts of precipitation over North America is largest (smallest) for February (January), with similar results in uncoupled mode. A key finding is that the relatively poor January skill is the result of the model placing the main circulation anomaly over the northeast Pacific slightly to the west of the observed, resulting in precipitation anomalies that lie off the coast instead of over land as observed. In contrast, during February the observed circulation anomaly over the northeast Pacific shifts westward, lining up with the predicted anomaly, which is essentially unchanged from January, resulting in both the observed and predicted precipitation anomalies remaining off the coast. Furthermore, the largest precipitation anomalies occur along the southern tier of states associated with an eastward extended jet—something that the models capture reasonably well. Simulations with a stationary wave model indicate that the placement of January El Niño response to the west of the observed over the northeast Pacific is the result of biases in the January climatological stationary waves, rather than errors in the tropical Pacific El Niño heating anomalies in January. Furthermore, evidence is provided that the relatively poor simulation of the observed January climatology, characterized by a strengthened North Pacific jet and enhanced ridge over western North America, can be traced back to biases in the January climatology heating over the Tibet region and the tropical western Pacific.

KEYWORDS: Climate variability; El Nino; Seasonal forecasting; Climate models; Model evaluation/performance; Reanalysis data

1. Introduction

ENSO teleconnections, manifested as large-scale waves in the atmosphere forced by tropical sea surface temperature (SST) anomalies, play a dominant role in determining the interannual variability of cold season precipitation and temperature over North America (Horel and Wallace 1981; Rasmusson and Wallace 1983;

Supplemental information related to this paper is available at the Journals Online website: https://doi.org/10.1175/JCLI-D-19-0841.s1.

Corresponding author: Young-Kwon Lim, young-kwon.lim@nasa.gov

DOI: 10.1175/JCLI-D-19-0841.1

Ropelewski and Halpert 1986; Kumar et al. 1996; Hoerling et al. 1997; Gershunov and Barnett 1998; Trenberth et al. 1998; Seager et al. 2010; Yang and DelSole 2012). In particular, these large-scale teleconnections modulate the atmospheric pressure and circulation over the northeast Pacific and the United States, causing ENSO-related anomalous weather events to occur across much of the United States (Horel and Wallace 1981; Hoskins and Karoly 1981; Webster 1981; Philander 1983; Rasmusson and Wallace 1983). The tropical Northern Hemisphere (TNH) and Pacific–North American (PNA) patterns (Barnston et al. 1991) are good examples of teleconnections known to influence the boreal winter climate over North America during ENSO events. In view of the key role of ENSO teleconnections, it is clearly very important to gain a full understanding of the extratropical response to ENSO over North Pacific and North America, with the ultimate goal of improving seasonal predictions of North American precipitation and temperature.

There is evidence that the boreal cold season atmospheric responses to ENSO SST, as well as the SSTs themselves, are not constant but vary during the course of the season (Jong et al. 2016; Chen et al. 2017), defined here as the months December through March (DJFM) following Chen et al. (2017). Furthermore, recent results based on the suite of North American Multi-Model Ensemble (NMME; Becker et al. 2014; Kirtman et al. 2014) forecasts suggest that there is a within-season monthly variation in skill during the boreal winter with most models showing significantly greater skill during ENSO events for February [at 1-month lead in 2-m air temperature (T2m) and precipitation over North America] compared with the neighboring winter months (Chen et al. 2017). Understanding the nature of such differences in prediction skill is important for advancing subseasonal and seasonal prediction, since it should provide clues as to the priorities for improving the prediction models and/or the initial conditions.

The apparent within-season monthly variation in ENSO-related prediction skill over North America during the cold season raises several important questions that will be addressed here: First, how different are the month-to-month ENSO responses during boreal winter over the Pacific–North America region? Previous studies indicate that North American precipitation and temperature responses related to ENSO do appear to change during the boreal winter (Jong et al. 2016; Chen et al. 2017). Second, what is the physical mechanism that induces this monthly variation in the ENSO response—is it, for example, related to changes in the SST or changes in the basic state of the atmosphere? Given the answers to those questions, the ultimate question to answer is how this leads to monthly variations in prediction skill.

To simplify matters, we will focus in this study on the El Niño response and North American precipitation. It is important to keep in mind that to some extent we are addressing second-order errors (i.e., the response to the first-order changes such as mean circulation)—although, as we shall show, these errors are quite consequential when one is concerned with improving subseasonal and seasonal predictions on a regional scale, such as over western North America. Many global models, in fact, already do produce a fairly realistic response to El Niño forcing when viewed on a global scale through the filter of seasonal averages (e.g., Joseph and Nigam 2006; Meehl and Teng 2007). Here we will show that that achievement, while representing substantial progress, is likely insufficient for advancing prediction skill on subseasonal and even seasonal scales. As it turns out, while predictions for February do indeed appear to be more skillful than those for the other winter months, the more pressing question is why January predictions are so much worse.

Our approach involves examining some of the key aspects of the January and February forecasts, starting with the ability of the model to represent the tropical El Niño heating distributions, the subsequent extratropical responses over the northeast Pacific, and the underlying atmospheric basic states within which the El Niño responses take place. Earlier studies demonstrated that the ability of global models to reproduce the extratropical Rossby wave response (including ENSO teleconnections) depends on the quality of the tropical heating and associated upper-tropospheric flow anomalies (Jin and Hoskins 1995; Yasui and Watanabe 2010; Weare 2013). However, an accurate representation of the basic state is also important (Ting and Sardeshmukh 1993; Dawson et al. 2011; Henderson et al. 2017). As such, we believe that understanding the nature of the relatively poor prediction skill of the El Niño–related precipitation anomalies over North America in January requires that we examine in some detail the impact and nature of the model's biases in the climatological basic state (in particular over the North Pacific). Specifically, we focus here on the possibility that errors in the climatological diabatic heating across the tropical Pacific and the Indian Ocean, as well as over the extratropical Tibetan Plateau region, play a role. While errors in tropical diabatic heating are the likely candidates to consider, the Tibetan Plateau is known to also modulate the large-scale atmospheric mass/circulation responses across the North Pacific during boreal winter (Lin and Wu 2011; Liu et al. 2017).

The remainder of this paper is organized as follows. Section 2 describes the model experiments, as well as the reanalysis and observational data employed in this study. Section 3 describes the results, followed by the summary and concluding remarks in section 4.

2. The model experiments and observational data

Addressing the above questions requires an extensive database (multidecadal and reasonably large ensembles) of model forecasts/simulations, and corresponding observational data for verification. These are briefly described below.

a. *MERRA-2 and observed precipitation*

Our primary observational dataset is the Modern-Era Retrospective Analysis for Research and Applications, version 2 (MERRA-2; Gelaro et al. 2017). MERRA-2 was produced at a horizontal resolution of 0.625° longitude × 0.5° latitude. The key variables utilized here for analysis include the upper-tropospheric (300 hPa) geopotential height and wind, temperature at 500 hPa and the surface, sea level pressure (SLP), and the diabatic heating due to moist and turbulent mixing processes (GMAO 2019a,b). In the case of precipitation, we use the Global Precipitation Climatology Project (GPCP) data (Adler et al. 2003) for the same period (1980–2017). We focus on the El Niño cold season from December through March covering the period 1980 through 2017—a period common to MERRA-2, the uncoupled atmospheric general circulation model (AGCM) simulations, and the atmosphere–ocean coupled GCM (AOGCM) predictions. We will, in particular, examine El Niño composites consisting of the 11 El Niño winters 1982/83, 1986/87, 1987/88, 1991/92, 1994/95, 1997/98, 2002/03, 2004/05, 2006/07, 2009/10, and 2015/16.

Additionally, we use NOAA's global land precipitation (Chen et al. 2002) for the longer time period (1948–2019) to verify robustness of the observed El Niño precipitation composites calculated from GPCP precipitation.

b. *The AGCM simulations*

An ensemble of 10 AMIP-style (Gates 1992) simulations were run for the time period January 1980 through December 2017 using the Goddard Earth Observing System (GEOS) AGCM employed in the development of MERRA-2 (Molod et al. 2015; Collow et al. 2017). Initial conditions for each ensemble member were taken from different days of November 1979 during the MERRA-2 spinup period. The AMIP simulations were run with the same SST data, GHGs, and other forcing, as well as being run at the same resolution as that of MERRA-2. The only difference from MERRA-2 is of course that the simulations did not assimilate observations. This similarity offers the unique opportunity to assess how the observations influence various aspects of the model climate, but of course to the extent that any model errors are reflected in the reanalysis, they also have the potential to bias our assessment of model errors.

As described in Molod et al. (2015) and Gelaro et al. (2017), the MERRA-2 AGCM includes the finite-volume dynamical core of Putman and Lin (2007), which uses a cubed sphere horizontal discretization to allow relatively uniform grid spacing at all latitudes. This AGCM was run at an approximate resolution of 0.625° longitude by 0.5° latitude and 72 hybrid-eta levels from the surface to 0.01 hPa. The upgrades to the physical parameterization schemes in the MERRA-2 AGCM include increased re-evaporation of frozen precipitation and cloud condensate, changes to the background gravity wave drag, and an improved relationship between the ocean surface roughness and ocean surface stress. More details about the AGCM components including convective process (Moorthi and Suarez 1992; Bacmeister and Stephens 2011; Lim et al. 2015), cloud microphysics (Bacmeister et al. 2006; Barahona et al. 2014), land surface process (Koster et al. 2000), glaciated land (Cullather et al. 2014), and the Goddard Chemistry Aerosol Radiation and Transport (GOCART) (Colarco et al. 2010) can be found in Molod et al. (2015). In the following we shall refer to these runs (10 members) for the period 1980–2017 as the M2AMIP simulations.

c. *The AOGCM predictions*

The Global Modeling and Assimilation Office (GMAO) currently produces an ensemble of 10 nine-month forecasts using the GEOS Subseasonal to Seasonal version 2 (GEOS S2S-2) fully coupled prediction system for delivery to the North American Multi-Model Ensemble (Kirtman et al. 2014) project every month. The 10 ensemble members are produced by initializing the model every five days prior to the start of the month, except for the date closest to the start of the month when additional forecasts are generated by perturbing the initial state. The perturbations were produced using a simple scaled differencing approach involving nearby (in time) atmosphere and ocean states. In addition to the forecasts, the GMAO produced a suite of hindcasts (four members) used to calibrate/bias-correct the forecasts and assess forecast skill. In the following we focus on the 1-month-lead boreal winter predictions for the period 1981–2017, and we shall refer to them as the FCST runs.

The GEOS S2S-2 AOGCM consists of the GEOS AGCM (an upgraded version from that used to produce the M2AMIP simulations, and including the catchment land surface model and GOCART), and the MOM5 ocean model developed by the NOAA Geophysical Fluid Dynamics Laboratory (Griffies 2012). All components of the AOGCM are coupled together using the Earth System Modeling Framework (ESMF). Further details about the AOGCM including the flux exchanges between ocean and atmosphere, sea ice model (Hunke and Lipscomb 2008), a coupled atmosphere–ocean data assimilation system, and the forecasts can be found in Molod et al. (2020).

d. *The SWM experiments*

The stationary wave model (SWM) is used (in section 3b) to address the question of whether the biases in the El Niño response over the North Pacific/North America region stem from biases in the stationary wave forcing or biases in the mean basic state. It is used again (in section 3c) to help isolate the source of the biases in the climatological January stationary waves. The SWM [described in detail in Ting and Yu (1998)] is the dry dynamical core of an AGCM with 14 unevenly spaced vertical levels in sigma coordinates and R30 truncation in the horizontal. The basic model variables include vorticity, divergence, temperature and surface pressure. A rigid-lid boundary is applied at both the top and the surface of the model atmosphere. Rayleigh friction and Newtonian cooling are applied in the vorticity, divergence, and temperature equations to represent turbulent momentum and heat transfer in the boundary layer, while biharmonic diffusion is applied to the free troposphere to crudely represent gravity wave drag. These damping coefficients are necessary to ensure meaningful SWM solutions.

For our experiments in section 3b, the SWM is forced by an estimate of the observed (composite mean) monthly diabatic heating/cooling[1] or model-produced heating/cooling that occurred during the El Niño cold seasons. In particular, we examine the response to the tropical El Niño heating/cooling anomalies in three different regions consisting of 1) the tropical central-eastern Pacific, 2) the tropical western Pacific/Maritime Continent, and 3) the eastern Indian Ocean (see Table 1 and dashed-line boxes in Fig. 5 for longitude/latitude boundaries of these regions). The atmospheric basic state used in the SWM is the three-dimensional climatological monthly mean taken from MERRA-2, the M2AMIP simulations, or the FCST runs.

In section 3c, we force the SWM with the January or February climatological heating anomalies (departure from the DJFM mean) over four different regions, consisting of three tropical regions (the Indian Ocean, the western Pacific, and the eastern Pacific) and, in the extratropics, a region encompassing Tibet (see Table 1 for longitude/latitude boundaries of these regions). All experiments have the same basic state consisting of the DJFM mean computed from MERRA-2, while the January and February heating anomalies are estimated from either MERRA-2 or the M2AMIP simulation.

TABLE 1. Longitude/latitude boundaries of each of the subregions defined in the text.

Names	Longitude/latitude boundaries
Tropical central-eastern Pacific	160°E–90°W, 10°S–10°N
Tropical western Pacific/Maritime Continent	120°–160°E, 0°–15°N
Eastern Indian Ocean	80°–120°E, 0°–15°N
Indian Ocean	60°–120°E, 15°S–15°N
(Tropical) western Pacific	120°E–180°, 15°S–15°N
(Tropical) eastern Pacific	180°–120°W, 15°S–15°N
North Pacific	120°E–120°W, 15°–70°N
Northeast Pacific	160°–130°W, 40°–60°N
Tibet	70°–100°E, 25°–40°N

Table 2 summarizes the observational data and models described in this section.

3. Results

a. *The observations and model simulations*

Figure 1 shows the spatial pattern correlations between the observed (GPCP) and simulated monthly precipitation (M2AMIP and FCST) anomalies over the North American region (180°–60°W, 15°–60°N) during the El Niño cold season. Recall that the FCST values are one-month lead AOGCM ensemble mean predictions, and the M2AMIP results are the ensemble mean of 10 AMIP simulations initialized in 1979. The spatial pattern correlations in December, February, and the DJFM average are within the range of 0.59 and 0.73, indicating a reasonably good capability of the models to reproduce the observed precipitation anomalies. In contrast, the correlation is substantially lower in January compared with the other three months (0.08–0.27). It is important to remember that these results are not peculiar to the GMAO models. Chen et al. (2017) reported that, for El Niño events in particular, the skill of one-month lead forecasts of North American precipitation with the NMME models[2] tends to be greater during February

---

[1] The heating is estimated from MERRA-2 and consists of the heating from the moist physics (e.g., latent heating) and turbulent mixing schemes.

[2] This includes the NASA predictions, but with an earlier version of the forecast system (GEOS S2S version 1; Borovikov et al. 2019) than that analyzed here.

TABLE 2. Brief summary of observational data and models used in this study.

	NOAA precipitation	GPCP	MERRA-2	AGCM (M2AMIP)	AOGCM (FCST)	SWM
Property	Observed precipitation	Observed precipitation	Reanalysis	Atmospheric GCM (uncoupled)	Atmosphere–ocean coupled GCM	Stationary wave model
Horizontal grid spacing of the output	0.5° × 0.5°	0.5° × 0.5°	0.625° × 0.5°	0.625° × 0.5°	0.5° × 0.5° (both atmosphere and ocean)	3.75° × 2.25°
No. of vertical levels			42	72	Atmosphere: 72, ocean: 40	14 (sigma)
No. of ensemble members				10	4	
Investigation period	1948–2019			1980–2017		

(compared with the surrounding boreal winter months), with forecasts for January tending to be considerably less skillful. In fact, this study was motivated by those results. Furthermore, since very similar results are obtained with the M2AMIP AGCM, it is also evident that this is not fundamentally a coupled model problem.

To get a better understanding of the above results we next look at the underlying precipitation anomaly patterns that lead to the differences in the correlations. Furthermore, to simplify matters we will focus on the relatively large differences between the January and February skill. Figure 2 shows that substantial differences occur between the observed (GPCP) and model results in January, particularly along the west coast of the United States and southern Canada, where the observations show strong positive anomalies (Fig. 2a) and the model results indicate mostly negative anomalies (Figs. 2b,c). In addition, the model (especially for M2AMIP) does not reproduce faithfully the observed wetness over the southwestern United States. The models also show a tendency for positive precipitation along the southern Alaskan coast while the observations show weak negative anomalies there. This contrasts with February (Figs. 2d–f), where the observations and model simulations are in agreement in producing overall weak anomalies along the coast (i.e., positive anomalies in the southern Alaska coast and the southwest United States, and slightly negative anomalies in the U.S. Pacific Northwest). Over the southeast United States, the positive anomalies are present in the model simulations during January. However, they are less so in the observations, which tend to show the weak positive anomalies with less intrusion onto the coast (Figs. 2a–c). In February, all three results show significant positive precipitation anomalies over the southern United States (especially the southeast) with negative anomalies encompassing the Ohio River Valley and the Great Lakes region, indicating better performance of the models for February.

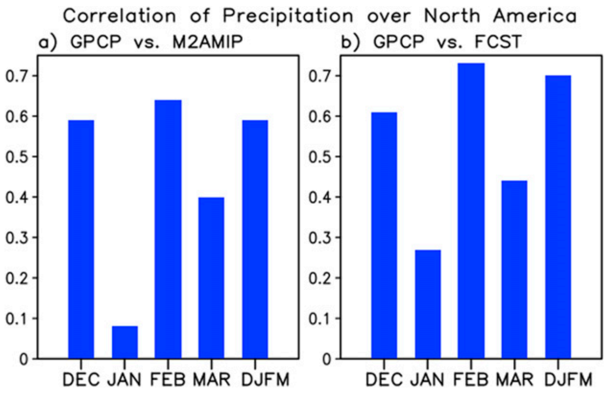

FIG. 1. The spatial correlations for the months of December, January, February, and March and the DJFM average between the precipitation composite anomalies computed from (a) GPCP and M2AMIP and (b) GPCP and FCST. The composites are the averages of the 11 El Niño winters that occurred during the period 1980–2017. The spatial domain for computing correlations is only land points over the region 180°–60°W, 15°–60°N, which encompasses Mexico, most of Canada except the polar region, and the United States including southern Alaska.

Focusing on the month-to-month precipitation changes (Figs. 2g–i), an increase over the southeastern United States is larger in observation with statistical significance.[3] It is clear that the lack of an appreciable change in the model outputs (Figs. 2h,i) over the southeastern United States, to a large extent, reflects the overestimation of precipitation in that region in January. The western part of the North America is another region

---

[3] Statistical significance is determined using a Monte Carlo approach in which the null hypothesis is that January is no different from February, allowing us to pool all the months together and then repeatedly (1000 times) randomizing them to generate different sets of 11 El Niño winter months.

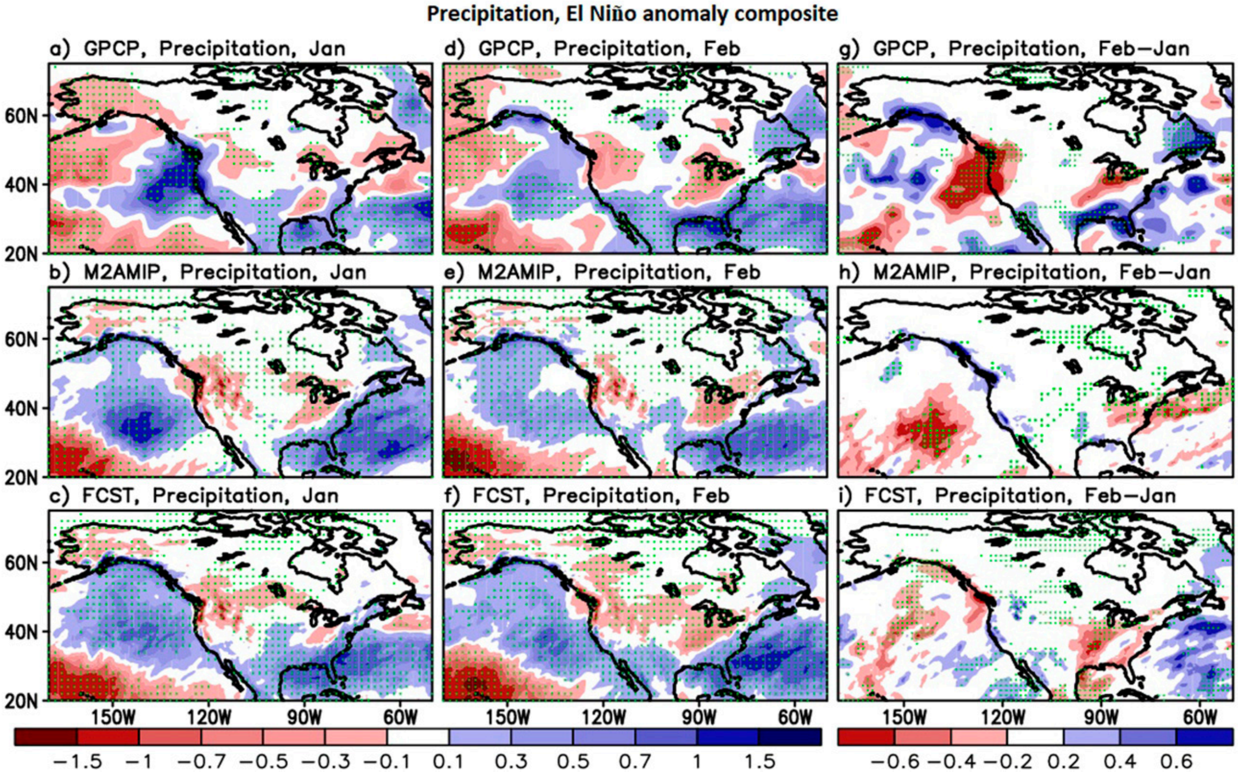

FIG. 2. The spatial patterns of the anomalous El Niño composites of the precipitation (mm day^{-1}) from the (top) GPCP, (middle) M2AMIP runs, and (bottom) FCST runs for (a)–(c) January and (d)–(f) February. The anomalies are computed with respect to the long-term mean for the period 1980 through 2017. The composites are the averages of 11 El Niño events that occurred during that period (see text for details). (g)–(i) Month-to-month precipitation change (February minus January). Green dots represent the grid points where the anomalies (left and center panels) and the difference between February and January (right panel) are significant at 90% confidence based on a Monte Carlo test.

where the January to February change in precipitation is larger in the observations than for the model results (Figs. 2g–i). Given the above results, it appears that the key regions where we need to explain the lack of agreement between the models and observations occur along the west coast of North America and along the southern tier of the United States, especially in the southeast.

For additional verification of the robustness of the observed month-to-month precipitation changes seen in Fig. 2, we have conducted the same calculation using NOAA's global land precipitation (Chen et al. 2002) for the longer time period 1948–2019 (now with 24 El Niño events rather than the 11 that occurred since 1980). As seen in Fig. S1 in the online supplemental material, the main January (February) anomalies including more (less) precipitation over northwest United States and southwest Canada, less (more) precipitation over southern Alaska, and less (more) precipitation over the southeast United States are reproduced, consistent with those in Figs. 2a, 2d, and 2g. This suggests that the precipitation differences between the two months obtained from the 11 El Niño cases are very likely not simply a result of sampling.

We next focus on the January to February circulation changes, with the hope that they can provide some insights into the nature of the precipitation changes. In January, the MERRA-2 anomalies of 300-mb (1 mb = 1 hPa) eddy height and SLP (Fig. 3a) are dominated by strong negative anomalies in the northeast Pacific, associated with the deepening of the Aleutian low (Schonher and Nicholson 1989), quite close to the west coast of the North America, providing favorable conditions for the transport of moist oceanic air to western North America and leading to enhanced precipitation along the coast (Fig. 2a). In February, however, the center of the negative geopotential height and the SLP anomalies over the northeast Pacific retreat to the west (Fig. 3d), producing less favorable conditions for precipitation over the western United States and Canada than in January. The negative height anomaly acts to direct southerly flow along its eastern flank to the southern coast of Alaska, leading to positive precipitation anomalies

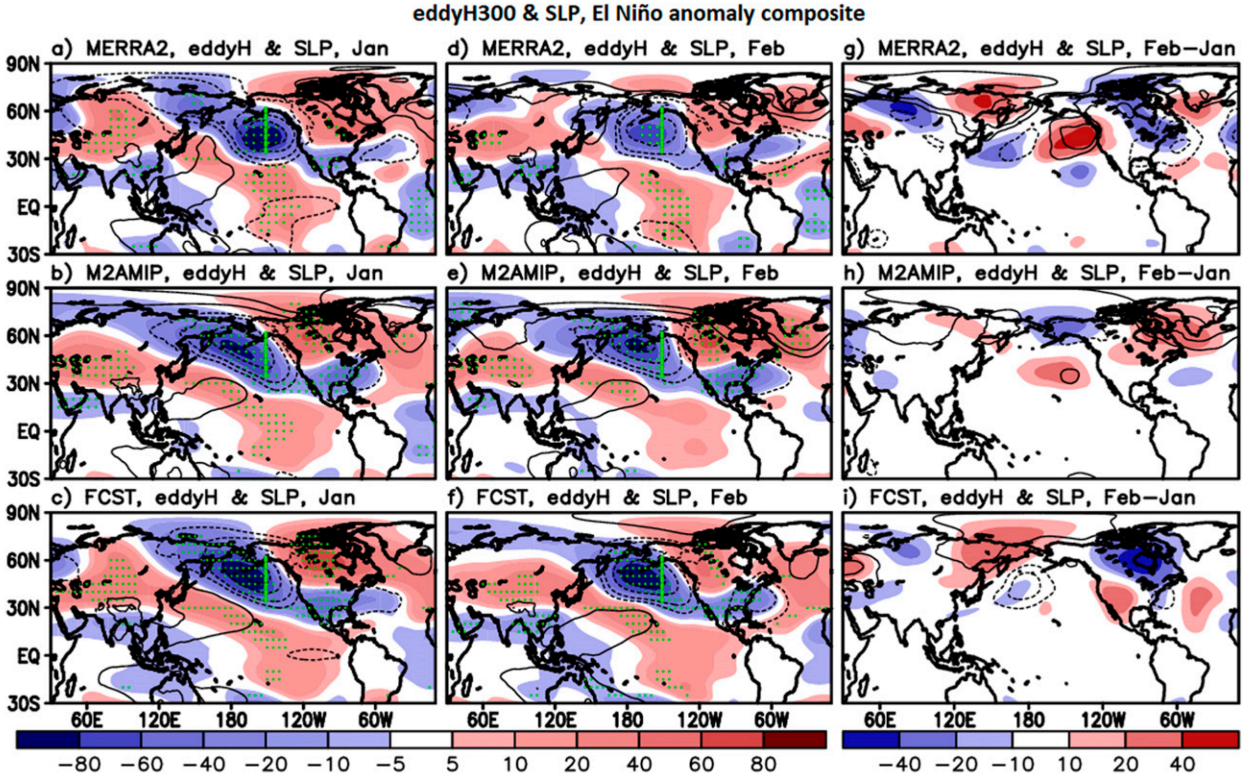

FIG. 3. As in Fig. 2, but for the anomalies of 300-mb eddy height (m; shaded) and sea level pressure (contoured; hPa), and where the top panels are based on MERRA-2. Dots are plotted on the grid points where the 300-mb eddy height anomalies are significant at 90% confidence. The vertical green lines over the northeast Pacific in (a)–(f) are positioned at the same longitudes in those panels (centered on the observed negative eddy height anomaly for the case of the January).

there (cf. Figs. 2a,d). While these January to February changes in the height and SLP anomalies are rather subtle on a global scale, they clearly have substantial impacts on regional precipitation. In fact, it has been noted in a number of earlier studies that the precipitation over the western North America is very sensitive to the precise location and intensity of this negative geopotential height anomaly (e.g., Schonher and Nicholson 1989; Ely et al. 1994; Jong et al. 2016).

This observed January to February change in the eddy height and SLP anomalies in the northeast Pacific is not reproduced by the M2AMIP or FCST runs (Figs. 3b,c,e,f,h,i). Specifically, the February eddy height and SLP anomalies in the northeast Pacific produced by the model runs (Figs. 3e,f) are remarkable for the lack of change in their positions from January. In fact, both the January and February predicted negative anomalies resemble the observed February anomalies over the northeast Pacific, making the prediction skill relatively greater for February, with the models failing to reproduce the observed location of the anomalies close to the west coast during January.

Earlier studies have shown that another key feature of the El Niño extratropical response over the North Pacific is the eastward extension and southward displacement of the North Pacific subtropical jet stream, leading to above normal precipitation to the southern tier of the United States, including southern California and Texas and extending to the southeast (e.g., Ropelewski and Halpert 1986; Trenberth et al. 1998; Mason and Goddard 2001; Seager et al. 2010). This strengthening and extension of the jet (to the northeast of Hawaii) is clearly evident in the MERRA-2 results for January (Fig. 4a) and presumably reflects the enhanced negative height anomaly in the northeast Pacific discussed above. During February, that westerly wind anomaly weakens; a rather subtle but key change from January is a further increase in the westerly wind anomalies along the southern border of the United States (Figs. 4d,g). It is likely that that strengthening of the jet (and the associated enhanced storminess; see, e.g., Schubert et al. 2008) plays a key role in producing the larger (compared with January) positive precipitation anomalies along the southern tier of states and much of the east coast (Figs. 2d,g).

The models fail to reproduce the observed strong westerly wind maximum over the eastern Pacific during

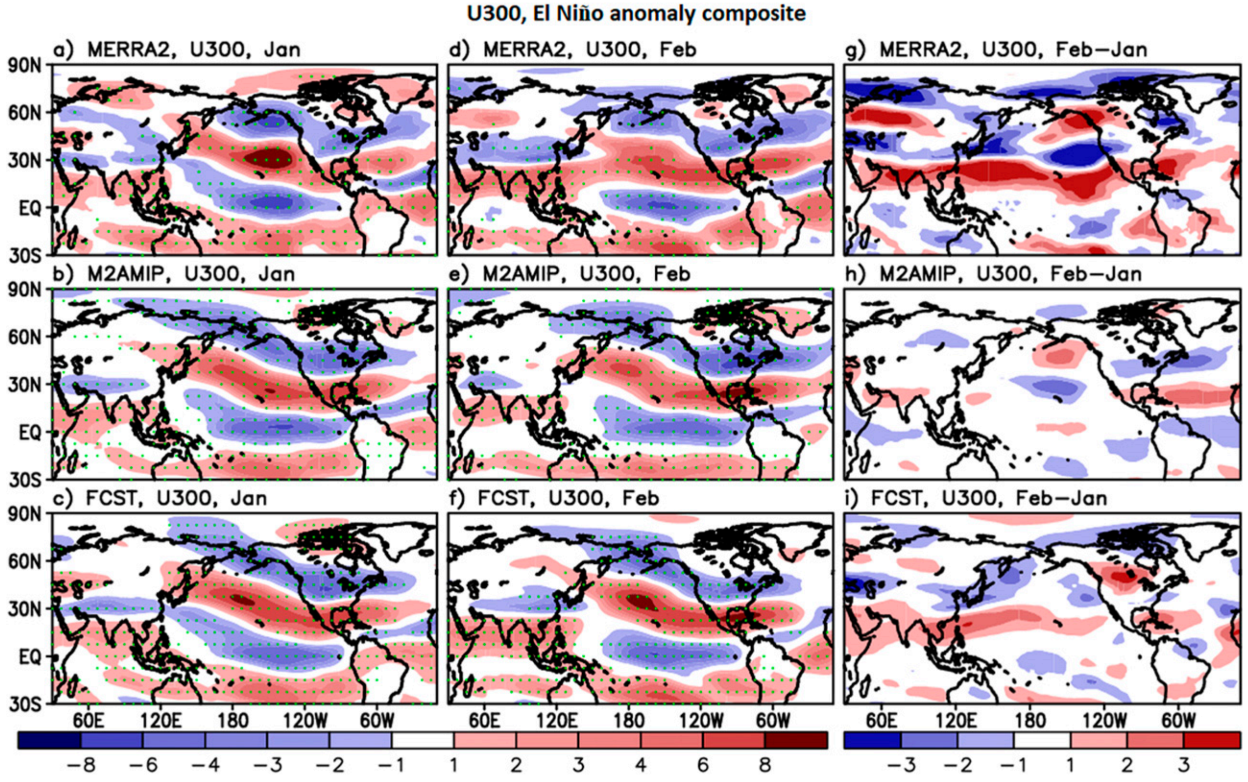

FIG. 4. As in Fig. 3, but for the 300-mb zonal wind (m s^{-1}) anomaly.

January (Figs. 4b,c). Here again the model results for January and February look more similar to each other than is observed, with both months resembling the observed February results. The model results in February do show some enhancement of the westerly wind anomalies along the southern tier of states (compared with January), although much less so than in the observations (Figs. 4g–i), due to the overestimation of the westerlies in that region in January (Figs. 4b,c). This early (January) enhancement of the westerly wind by the models likely contributes to the overestimated positive precipitation anomaly over the southeastern United States in January as shown in Figs. 2a–c. It is also noteworthy that the observed negative precipitation anomalies over the Great Lakes/Ohio River Valley (Figs. 2a,d) appear to be linked to the negative zonal wind anomalies that extend southwestward from the North Atlantic across northern United States (Figs. 4a,d). These negative zonal wind anomalies tend to be reproduced well by models (Figs. 4b,c,e,f).

The above results suggest that the better skill in the precipitation forecasts in February (compared with January) is primarily the result of a fortuitous lack of change in the position of the negative height anomaly in the northeast Pacific (it is off the coast for both months but observed to be off the coast only in February), and the fact that the extension of the jet along the southern tier of states (reasonably well predicted by the model in February) produces a substantial amount of the February rainfall. Therefore, a key model deficiency that needs explanation is the lack of the longitudinal shift of the negative height anomaly in the northeast Pacific and, in particular, the reasons behind the failure of the model to reproduce the location of that anomaly (close to the west coast) during January. We next examine this issue employing a SWM.

b. SWM results

In this section, we examine the extratropical response to El Niño over the North Pacific and North America using a SWM (see section 2d for a description of the SWM and experiments) with a focus on identifying the main cause of the differences between the January and February circulation responses over the North Pacific and North America found in the observations. A key question we aim to address is whether the observed January/February differences are the result of a change in the El Niño tropical heating anomalies, a change in the basic state, or a combination of both. As addressed in section 1, the justification for this focus is based on

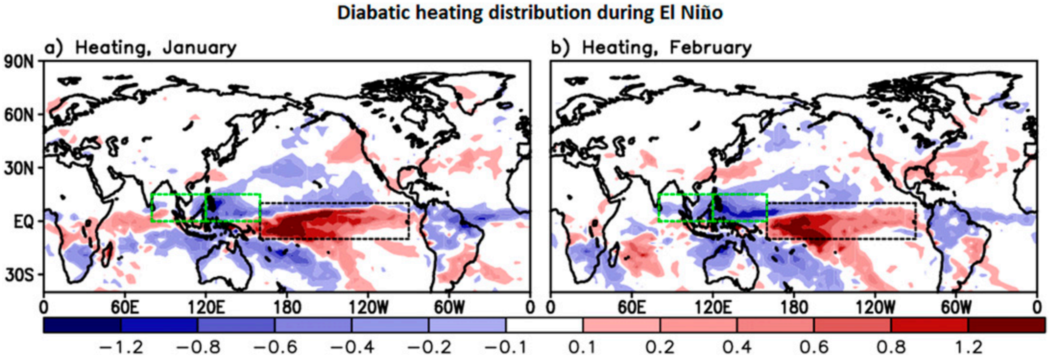

FIG. 5. Distribution of the El Niño diabatic heating (K day^{-1}) estimated from MERRA-2 for (a) January and (b) February. The boxes indicate the location of the heating region used to force the SWM (e.g., Fig. 6). The heating is computed as a composite of 11 El Niño events covering the period 1980–2017.

earlier studies that have shown that the large-scale atmospheric circulation structures over the North Pacific and North America are strongly affected by the atmosphere/ocean conditions over the tropical Pacific (e.g., Horel and Wallace 1981; Hoskins and Karoly 1981). There is also evidence that heating anomalies over the Indian Ocean can induce a large-scale extratropical response, contributing to North American/North Atlantic climate anomalies (Hoerling et al. 2004).

We first examine the observed El Niño diabatic heating anomaly distributions during January and February (recall that these are estimated from MERRA-2). Figure 5 shows that the spatial patterns of the diabatic heat anomalies for both months exhibit the well-known spatial structure associated with El Niño consisting of large positive anomalies spanning the tropical central-eastern Pacific, with anomalies of opposite sign producing a horseshoe pattern and encompassing the far western Pacific including the Maritime Continent (Figs. 5a,b). The vertical profiles of the heating (not shown) tend to have a maximum in the middle troposphere, reflecting the major contribution from latent heating. Notable differences between the two months are that the large heating region over the tropical Pacific is confined to ~150°W in February, whereas it extends farther east to ~120°W in January. Over the western Pacific, the negative anomalies are centered over the Maritime Continent (specifically near the Philippines and east of Borneo island) during both months. In February, this negative anomaly enhances, extending to the east just north of New Guinea (Fig. 5b). Based on the overall spatial features, it can be concluded that, although the tropical diabatic heat anomaly distribution is roughly similar in the two months, the main anomalies over the central-eastern Pacific in January tend to be situated a little to the east of those in February.

We next use the SWM to examine the extratropical response to the January and February tropical heating anomalies (as estimated from MERRA-2). To assess the sensitivity of the extratropical responses (over the North Pacific and North America) to the monthly changes in heating and the basic state we carry out several different experiments. As already mentioned above, our main goal here is to see if we can identify the source(s) of the observed January/February shift in the negative height anomaly over the northeastern Pacific. As such, we first run the SWM forced by the main El Niño diabatic heating anomalies over the tropical central-eastern Pacific (see the boxes in Fig. 5). Here, two SWM experiments are carried out (see section 2d), one with the January heating anomaly and the other with the February anomaly, with each employing the climatological three-dimensional atmospheric basic state (taken from MERRA-2) for the corresponding month. The resulting SWM responses are shown in Figs. 6a and 6d (we show here the upper troposphere eddy[4] streamfunction, rather than eddy height, to be consistent with the SWM variables). Comparing those results with Figs. 3a and 3d, we see that the SWM (when forced with the central-eastern tropical Pacific heating anomalies) does a very reasonable job of reproducing the main observed circulation anomalies over the North Pacific and North America. Remarkably, it also reproduces the January/February differences in the location of the negative anomalies in the northeastern Pacific, with the January anomalies located closer to the coast.

To determine whether the shift is the result of heating differences or differences in the basic state, we next rerun the SWM experiments, but now switching the basic states between the two months. The results of those

---

[4] By *eddy*, we refer to the deviation from the zonal mean.

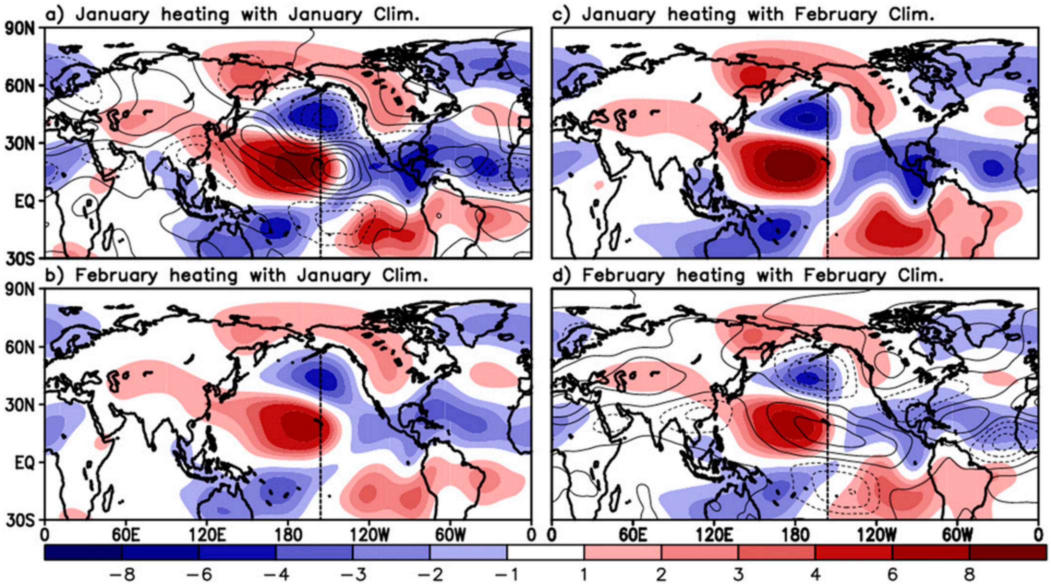

FIG. 6. The SWM streamfunction response (10^6 m^2 s^{-1}) in the upper troposphere ($\sigma = 0.257$) to the composite El Niño heating anomalies in the central-eastern tropical Pacific region (see the black dashed line boxes in Fig. 5), for the (a) January heating and January basic state, (b) February heating and January basic state, (c) January heating and February basic state, and (d) February heating and February basic state. The atmospheric basic states (1980–2017) and the estimates of the composite El Niño heating anomalies (based on 11 El Niño events; see Fig. 5) are from MERRA-2. Contoured in (a) and (d) are observed eddy streamfunction anomalies converted from eddy height anomalies in Figs. 3a and 3d. The vertical lines are positioned at the same longitudes in both sets of panels (centered on the negative streamfunction anomaly in the North Pacific for the case of the January heating and January basic state).

experiments (Figs. 6b,c) clearly show that the atmospheric response over the northeast Pacific close to the west coast in January is primarily determined by the basic state. For instance, when the SWM is forced with the January heating using the February basic state (Fig. 6c), the locations of the negative anomalies are more similar (shifted westward) to those for the February heating and the February basic state seen in Fig. 6d, although with somewhat stronger amplitude. When the SWM is forced with the February heating but with the January basic state (Fig. 6b), however, the main negative anomaly in the northeast Pacific (as well as the positive anomaly over western North America) remains close to the west coast, similar to the results for the January heating and January basic state in Fig. 6a, although with weaker amplitude. The above results demonstrate that the observed January/February zonal shift of the main streamfunction anomalies over the northeast Pacific and western North America is to a large extent controlled by the changes in the basic state, rather than any changes in the central-eastern tropical Pacific forcing.

To more directly assess the impact of errors in the model's climatological basic states, we repeat the SWM experiments but now using the January and February basic states determined from the M2AMIP runs,[5] although we again use the same MERRA-2 estimates of the heating anomalies used above. Figure 7 shows that all four experiments place the main streamfunction anomalies over the northeast Pacific and North America farther west, consistent with the position of the observed February anomalies. In particular, the runs with the January basic state (Figs. 7a,b) fail to reproduce the observed anomalies close to the coast as we see when using the observed January basic state (Figs. 6a,b). These results show quite clearly that it is the biases in the January basic state that are the main factor in producing the incorrect position (shifted to the west) of the circulation anomalies over the northeast Pacific and North America in January.

A further set of experiments was carried out to examine whether the results change if instead of using MERRA-2 estimates of the heating anomalies, we use M2AMIP-derived (ensemble mean) heating anomalies on top of the MERRA-2 basic state. The results, shown

---

[5] In what follows, for simplicity we focus on basic states obtained from the M2AMIP simulations, although very similar results are obtained based on the FCST states.

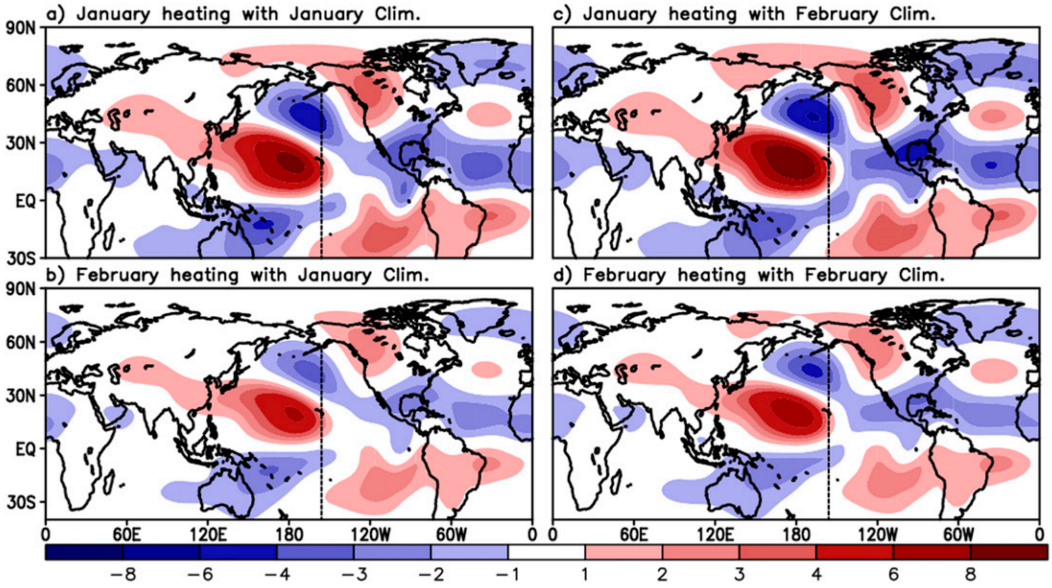

FIG. 7. As in Fig. 6, but for the atmospheric basic state taken from the M2AMIP run.

in Fig. 8, are overall consistent with Fig. 6 in terms of the location of the negative anomaly over the North Pacific, indicating that errors in the model diabatic heating contribute little to the difference in the response (i.e., the zonal shift) between the two months.

Additional SWM experiments are done forcing the model with the heating anomalies confined to the eastern Indian Ocean and the tropical western Pacific/ Maritime Continent (see green boxes in Fig. 5), with the regions chosen to assess the separate impacts of the main cooling anomalies over the western tropical Pacific warm pool, as well as the anomalies over the Indian Ocean. While these results (not shown) again produce large-scale wave trains across the North Pacific and North America, the amplitudes are considerably weaker than that obtained from the forcing in the central-eastern tropical Pacific. Hence, we conclude that it is the forcing in the central-eastern Pacific during El Niño

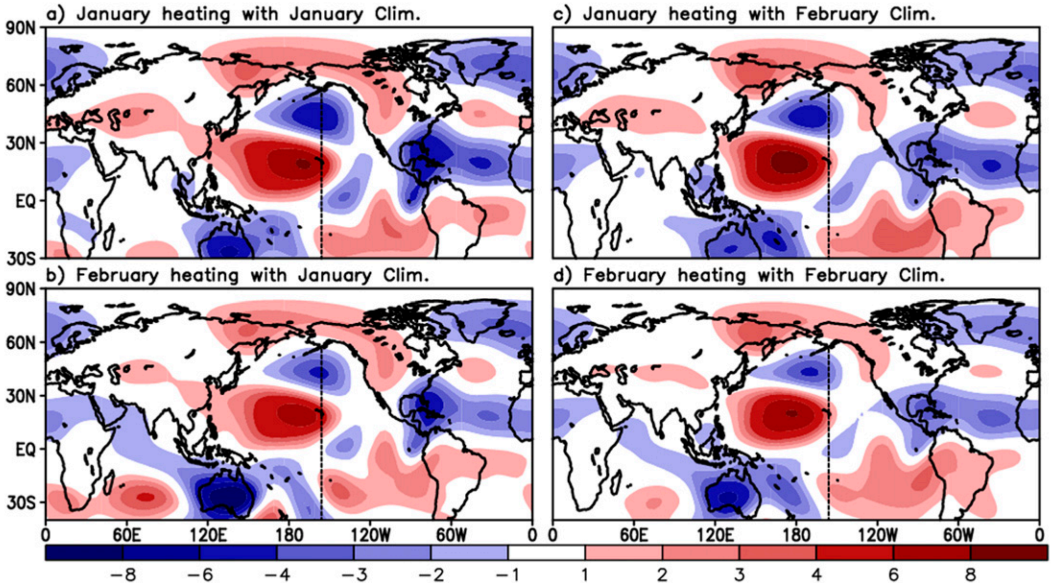

FIG. 8. As in Fig. 6, but for the composite El Niño heating anomalies as a diabatic heat source from the M2AMIP run.

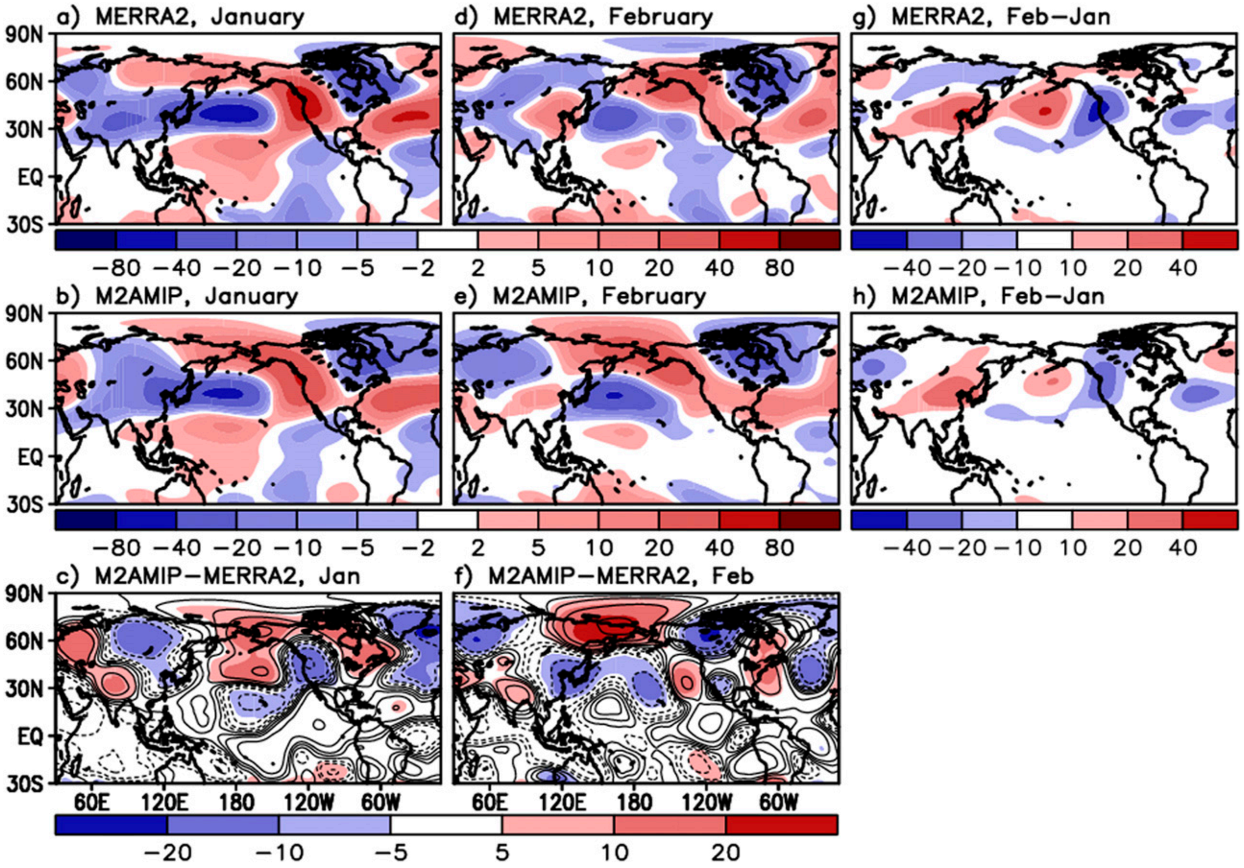

FIG. 9. Climatological variation of the 300-mb eddy height (m) in (a)–(c) January and (d)–(f) February from (top) MERRA-2 and (middle) M2AMIP. The monthly values here are the differences from the respective December through March means. (bottom) The difference between M2AMIP and MERRA-2. While shading represents the difference in the 300-mb eddy height, contoured are the differences in eddy streamfunction. (g),(h) The month-to-month change (February minus January) from MERRA-2 and M2AMIP, respectively.

that is primarily responsible for the remote response over the northeast Pacific and North America, consistent with previous studies (Horel and Wallace 1981; Philander 1983; Rasmusson and Wallace 1983).

In view of the central role of the biases in the January climatological basic state in producing the biases in the circulation anomalies and so presumably also the biases in the January precipitation response over North America, we next look into the possible sources of those biases in the basic state.

c. The January and February basic states

A key result concerning the model results described so far is the tendency for the models to show less within-season monthly variation than the observations. In particular, January and February tend to be very similar in terms of the El Niño responses over the northeast Pacific and North America (and those both tend to resemble the February observed response). Our SWM results suggest that the January and February climatological basic states must have important differences that lead to subtle but important shifts in the extratropical response to the El Niño tropical Pacific heating—and these differences in the climatologies are apparently not reproduced in the model. In this section we will look in some detail at the differences in the observed January and February climatologies, the possible causes of those differences, and why those are not well simulated.

The two top panels in Fig. 9 show the 300-mb eddy height climatologies for January and February from MERRA-2. Here we show the differences with respect to the December through March mean to more clearly show how January differs from February. The main features of the observed January climatology (Fig. 9a) over the North Pacific and western North America are a large positive anomaly located along the west coast (centered on the Pacific Northwest) with a negative anomaly to the west, extending across the North Pacific.

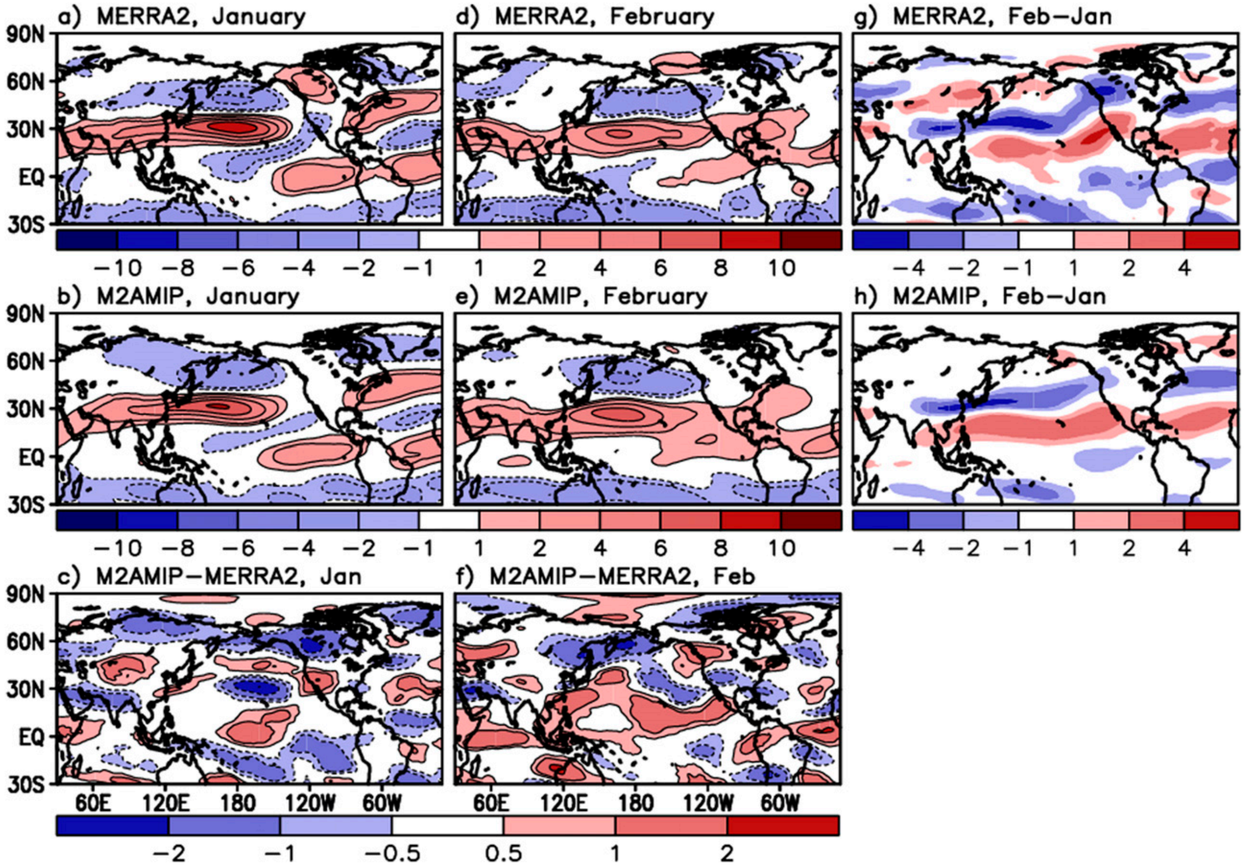

FIG. 10. As in Fig. 9, but for the 300-mb zonal wind (m s^{-1}).

The latter (together with a positive anomaly to the south) is consistent with a seasonal enhancement of the North Pacific jet (Fig. 10a). During February the anomalies are less pronounced (Fig. 9d), with a weaker positive anomaly along the coast (with maximum values now centered on the Gulf of Alaska) and negative anomalies over the North Pacific that have maximum values to the west of those in January.

The M2AMIP runs appear to do an overall credible job of reproducing the basic observed wave patterns (Figs. 9b,e). On closer inspection, however, it is clear that the model does not fully reproduce the observed intensity, with underestimation in January (Figs. 9a,b). Over the North Pacific and North America the model underestimates the strength of the January west coast ridge, as well as the north–south dipole upstream of that (Figs. 9b,c)—a reflection of the underestimation of the January strengthening of the Pacific jet at ~30°N (Figs. 10a–c). In February some of the largest differences occur at high latitudes north of about 60°N (Fig. 9f). Overall, the major biases found in January, which consist of the weak west coast ridge, the weak north–south dipole at the midlatitude North Pacific, and the related weak Pacific jet stream, are less evident in February (Figs. 9d–f and 10d–f). While our focus here is on the bias in the January climatology, as that was found to cause the erroneous El Niño response over the northeast Pacific (e.g., Fig. 7), we will come back to a discussion of the bias in the February climatology in section 4.

We now look at what might be driving the boreal winter January climatology in the observed stationary waves over the North Pacific and North America region (Fig. 9a), using the same SWM. Our intent here is not to try to fully reproduce the observed climatological stationary waves, but rather to get some sense of what is driving the climatological January changes, with respect to DJFM mean climatology, with the hope that this will give us a clue as to the model deficiencies responsible for the January biases (Fig. 9c). We begin by examining the response of the SWM to the observed January climatological diabatic heating anomalies (January minus the DJFM mean; Fig. 11c) in three different tropical regions (the Indian Ocean: 60°–120°E, 15°S–15°N, the western Pacific: 120°E–180°, 15°S–15°N, and the eastern Pacific: 180°–120°W, 15°S–15°N), as described in section 2d.

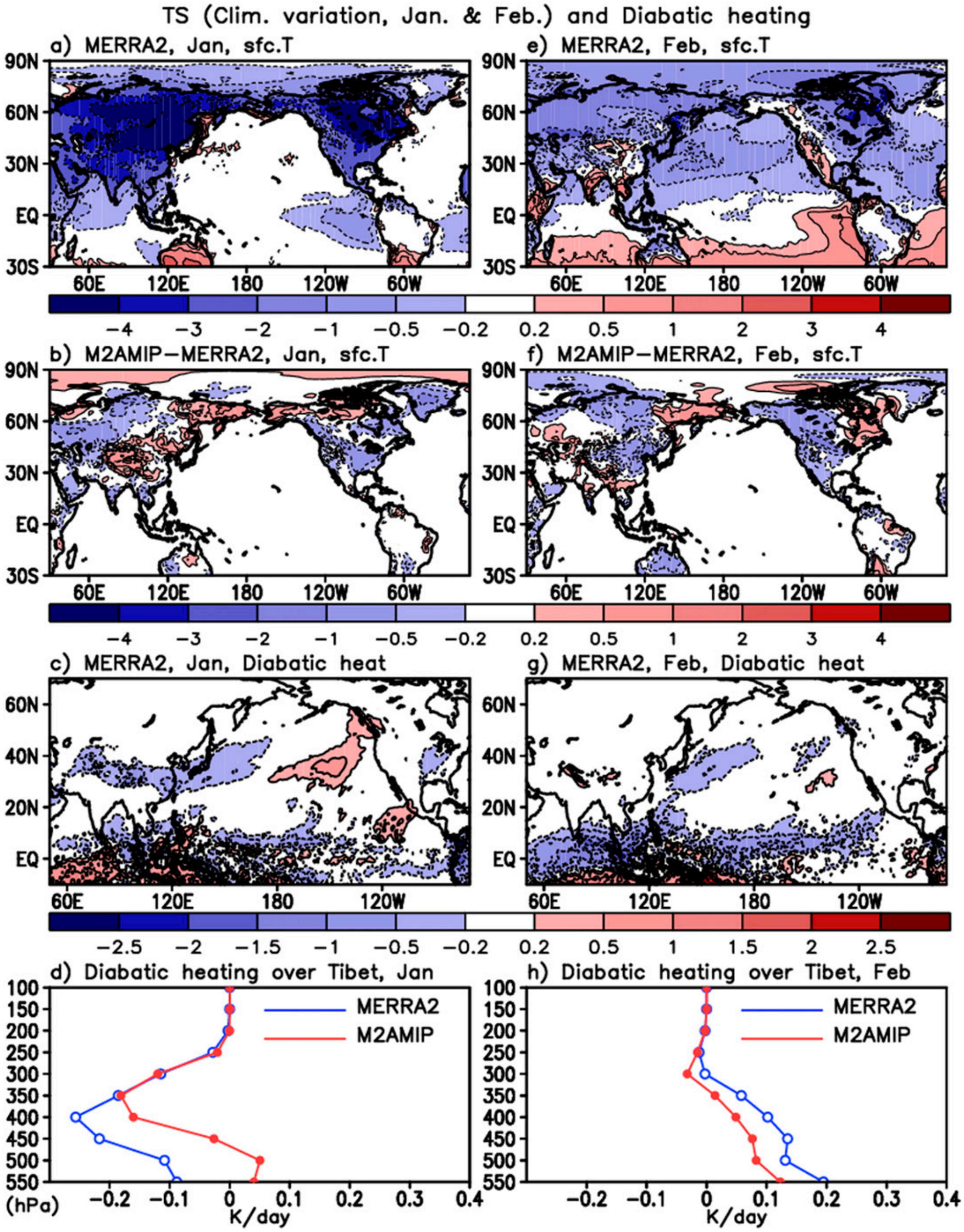

FIG. 11. Climatological variation of the surface temperature (°C) in (a) January and (e) February captured from MERRA-2. Differences in surface temperature between M2AMIP and MERRA-2 (M2AMIP minus MERRA-2) are plotted in (b) January and (f) February. Third panels from the top represent the estimated diabatic heating from MERRA-2 at midtroposphere (400 mb) (K day^{-1}) for (c) January and (g) February across the East Asian continent and Pacific. Bottom panels show the vertical profile of the diabatic heating in (d) January and (h) February over Tibet (the region is defined by the box shown in Fig. 12) from MERRA-2 (blue) and M2AMIP (red). The x axis represents the diabatic heating (K) and the y axis is vertical pressure levels (hPa). The seasonal average (December–March) has been subtracted from all quantities. All results are based on MERRA-2.

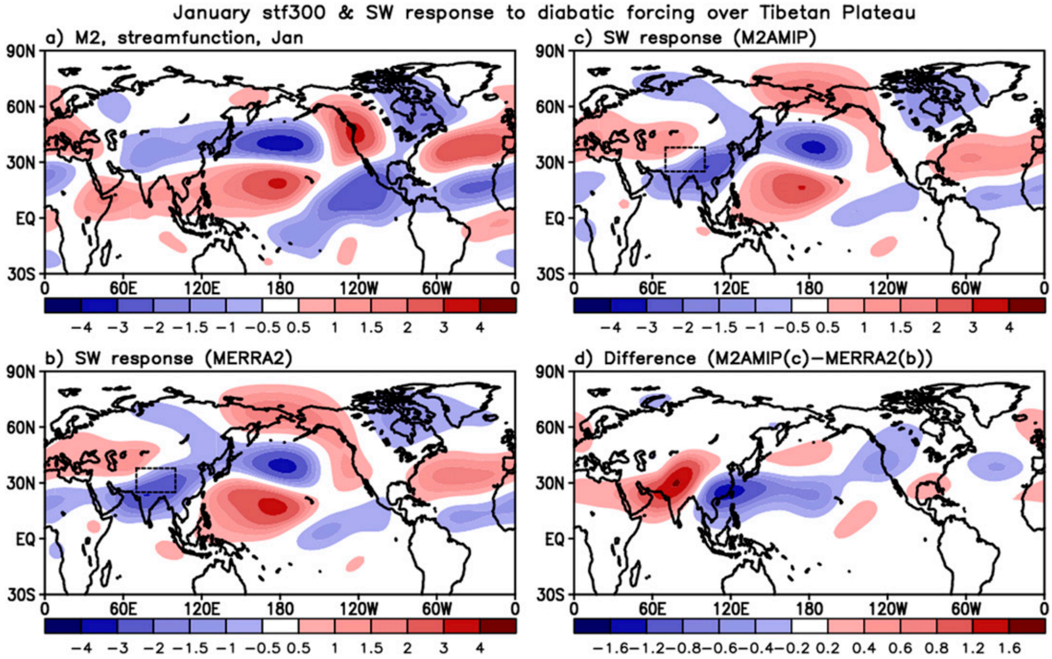

FIG. 12. (a) Climatological 300-mb eddy streamfunction ($10^6\ \mathrm{m^2\,s^{-1}}$) in January computed from MERRA-2. (b),(c) The streamfunction responses ($10^6\ \mathrm{m^2\,s^{-1}}$) in the upper troposphere ($\sigma = 0.257$) produced by the SWM forced with climatological January diabatic heating in the region of the Tibetan Plateau [outlined by the boxes in (b) and (c)]. In (b) and (c) the diabatic heating is estimated from MERRA-2 and M2AMIP, respectively. The atmospheric basic state is in both cases the climatology averaged from December through March computed from MERRA-2. (d) The difference in the SW responses between (c) and (b) [(c) minus (b)]. The December through March average has been subtracted from the January values in all cases.

Here the basic state employed in the SWM is the DJFM mean computed from MERRA-2. The results of those experiments (Fig. S2) indicate that the forcings from these tropical regions alone are unlikely to be the main drivers of the climatological January anomaly, in that the individual SWM responses do not bear a strong resemblance to the observed (upper-left panel of Fig. S2). In particular, the spatial correlations between the SWM responses and the observed January pattern computed over the region (120°E–120°W, 15°–90°N) that encompasses the North Pacific are −0.6, 0.37, and 0.34, for the diabatic forcing in the Indian Ocean, western Pacific, and eastern Pacific regions, respectively. Nevertheless, we will come back to the response to the western tropical Pacific as a possible important contributor to an overall response that includes forcing in a region outside the tropics.

In particular, based on the work of Lin and Wu (2011) and Liu et al. (2017) we look into the possible role of diabatic forcing in the Tibet region in driving the January climatology. Those studies concluded that strong Tibetan Plateau cooling may induce anomalous patterns of SLP and geopotential height over the North Pacific that resemble the positive phase of the PNA, similar to the patterns over the North Pacific in Figs. 9a and 9b. Here, we suspect that insufficient climatological January cooling over the Tibet region in the model could contribute to the differences seen in Fig. 9c. Figure 11 suggests that that might be the case. The top two panels (Figs. 11a,e) show that surface temperature is overall cooler in January compared with February over much of the NH landmasses including the Tibet region (in fact, it is the coldest of the December through March winter months over that region; not shown). It turns out that the diabatic cooling itself is also larger in January compared with February over the Tibet region (cf. Figs. 11c,g). Figures 11b and 11d show that the M2AMIP model is both too warm (Fig. 11b) and has insufficient cooling (extending up to about 400 mb; Fig. 11d) over the Tibet region. The heating distribution and bias is noticeably different in February, with the model exhibiting less diabatic heating bias compared with January over the Tibet region (Figs. 11f,h).

With those results in mind, we next perform the same January SWM experiment described earlier, but instead of tropical forcing, we now force the SWM with the observed (estimated from MERRA-2) January climatological cooling anomaly (January minus DJFM mean) over the Tibet region (the region outlined by the box in Fig. 12). The response (Fig. 12b) shows much greater

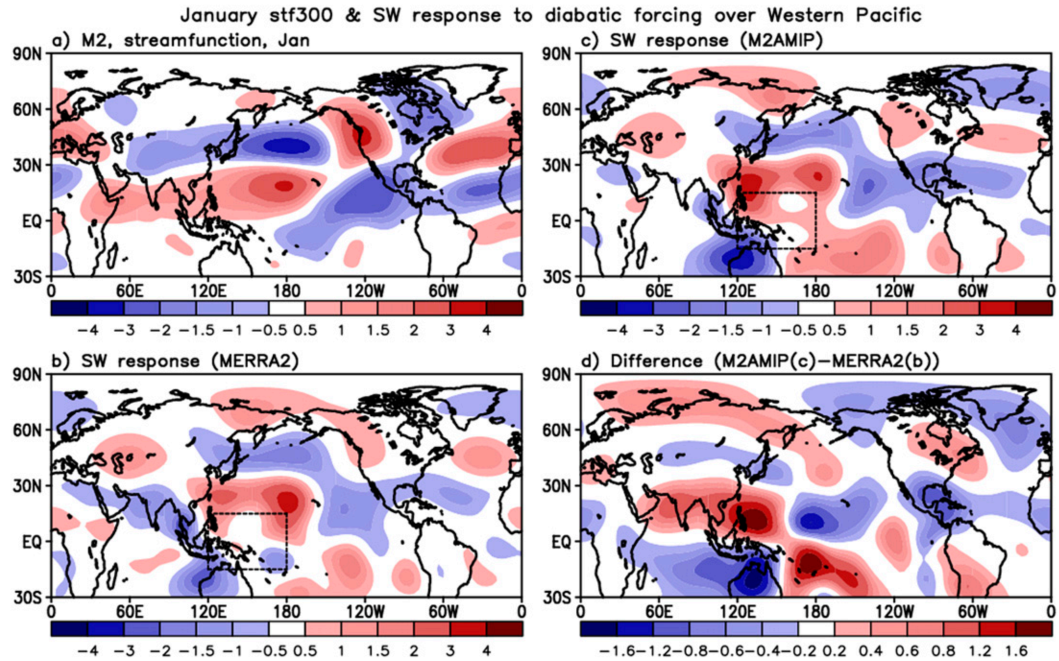

FIG. 13. As in Fig. 12, but for the diabatic heating in the region of the tropical western Pacific (120°E–180°, 15°S–15°N).

similarity to the observed January climatology anomaly (January minus DJFM mean) (Fig. 12a)[6] compared to that from the tropical forcing, with a spatial correlation between the two patterns of 0.76.

We next perform an additional SWM experiment, which is identical to the above, except that the diabatic forcing is that estimated from the M2AMIP model (Fig. 11d). Compared to the experiment in which the diabatic forcing is estimated from MERRA-2 (Fig. 12b), the SWM response in this case (Fig. 12c) shows a generally smaller amplitude. The difference field (Fig. 12d) clearly shows the weakening of the west coast ridge and meridional dipole over the North Pacific when using the M2AMIP forcing, generally consistent with the differences over the North Pacific that we see from the M2AMIP results in Figs. 9a–c, although the overestimation of the geopotential height over high latitudes (Alaska) is not reproduced.

The smaller magnitude of the values over the North Pacific in Fig. 12d compared with those in Fig. 9c indicates that there may be other factors that contribute to the January basic state bias. Here we again consider the impact of the heating in the tropical western Pacific. As we have already seen (Fig. S2, upper-right panel), the spatial pattern of the response to the tropical western Pacific heating source does resemble to some degree the observed January basic state over the midlatitude North Pacific although there is a small northward shift of the pattern over the North Pacific, compared to the observed. We see from Fig. 13 that the response to the observed (based on MERRA-2) January climatological heat source in the tropical western Pacific region (already shown in Fig. S2c, but repeated in Fig. 13b for convenience) and the response to the heat source in that same region but based on M2AMIP (Fig. 13c) produce different stationary wave responses over the North Pacific (Fig. 13d). We see that the distribution of the positive differences over the North Pacific north of 30°N and the negative values to the south in Fig. 13d bear some similarity to the north–south dipole of the January eddy streamfunction bias (Fig. 9c). Also, the quadrupole structure of the differences in the western tropical Pacific in Fig. 13d has a signature in the bias shown in Fig. 9c.

Finally, in Fig. 14 we show the stationary wave model response to the sum of the Tibetan heat source (Fig. 12) and tropical western Pacific heat source (Fig. 13). The difference distribution in Fig. 14d now shows an overall substantially greater similarity to model bias (Fig. 9c) than the individual responses alone, including the local response over the Tibet region, with the main exception being in the high latitudes over Alaska and the Bering Strait region.

---

[6] This is essentially the same as Fig. 9a but converted here to streamfunction to allow a more direct comparison with the SWM results.

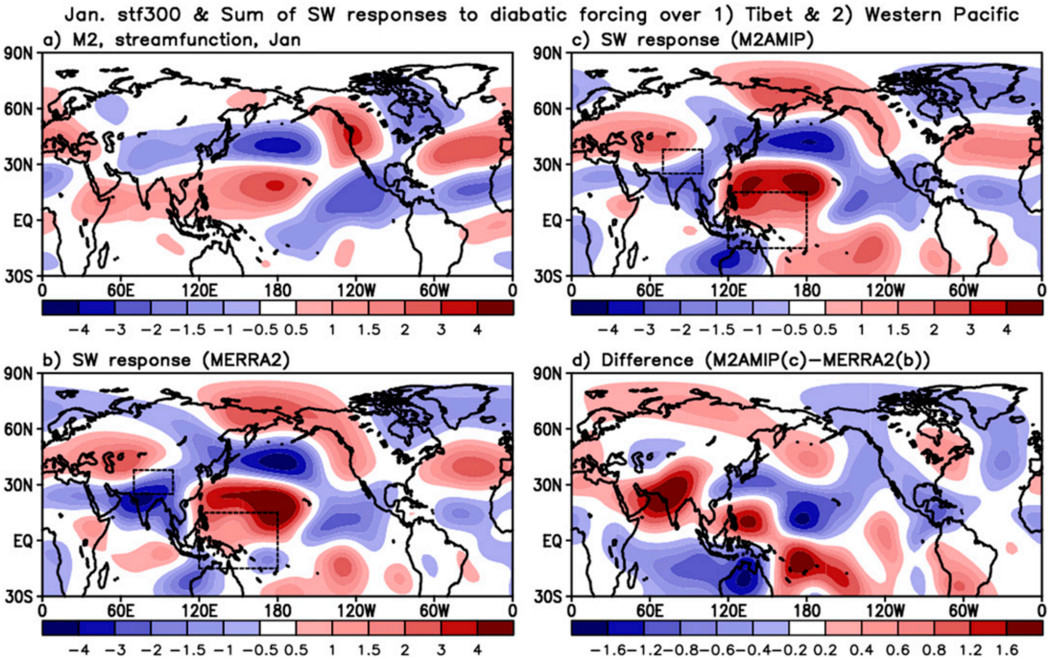

Fig. 14. As in Fig. 12, but for the results by the combined impact of diabatic heat source over Tibetan Plateau and tropical western Pacific [outlined by the boxes in (b) and (c)].

The above results suggest that biases in the January heating over the Tibet region (insufficient cooling) and the tropical western Pacific may be key factors in producing the M2AMIP model stationary wave biases over the North Pacific/North American region during January. While this is suggestive, we must however emphasize that more detailed investigation and experimentation is required employing a full AGCM or AOGCM to confirm these results.

4. Summary and concluding remarks

In this study we have addressed the question of why the January predictions of North American precipitation during El Niño events tend to be less skillful than the predictions for February. The study was inspired by Chen et al. (2017), who found that the skill of 1-month-lead T2m and precipitation forecasts over North America during ENSO in the NMME models (including the GEOS model, although an older version than the one examined here, GEOS S2S-1; Borovikov et al. 2019) tended to be greater for February compared with predictions for the neighboring winter months.

Our results show that the February predictions of precipitation over North America during El Niño are indeed more skillful than the predictions for the other winter months (spanning December through March) in both coupled (GEOS S2S-2 one-month lead predictions) and uncoupled (long AMIP-style simulations) versions of the GEOS model, although the more striking aspect of our results is just how much worse the January predictions are compared to the other winter months. As such we narrowed the scope of our investigation further by focusing on just the predictions for January and February. Furthermore, since the differences in skill do not appear to be associated with atmosphere–ocean coupling issues, we focused much of the analysis on long-term simulations made with the GEOS AGCM forced by observed SST (the M2AMIP runs).

It was shown that the skill of the North America precipitation predictions during El Niño is sensitive to relatively small phase errors in the prediction of the main circulation anomaly over the northeast Pacific characterized by a deepening of the Aleutian low. The model produces circulation anomalies that lie off the coast during both January and February, whereas that is only true for February in the observations. During January the observed circulation anomaly is situated farther east (compared to February) sitting just off the west coast, where it is responsible for producing the enhanced rainfall along the west coast during that month. This does not occur in February (the circulation anomaly is too far west); instead, an enhanced jet along the southern tier of states contributes to the positive precipitation anomalies there – something the model is able to reproduce reasonably well in February.

As such, it is clear that the key model deficiency that produces the poor precipitation skill over North America during January is that the El Niño circulation response over the northeast Pacific is situated too far off the west coast. Employing a SWM we have been able to show that this is the result of biases in the January climatological stationary waves, rather than errors in the January tropical Pacific heating anomalies. Additional experiments with the SWM suggest that the relatively poor simulation of the observed January climatology, characterized by a strengthened North Pacific jet and enhanced ridge over western North America, is due to biases in the January heating over the Tibet region and the tropical western Pacific.

While the February predictions of precipitation are considerably better than those for January, the February climatology over the North Pacific also exhibits biases, although these have a character different from those for January and do not appear to seriously alter the El Niño responses over the North Pacific (cf. Figs. 6 and 7). For January, it is the north–south dipole of the bias in the North Pacific (Fig. 9c) with a positive eddy height bias over the northeast Pacific that appears to be unfavorable for the development of the negative eddy height anomaly over that region associated with the extratropical El Niño response. Moreover, the biases in the eddy height anomalies over the northeast Pacific and west coast (Fig. 9c) drive anomalous winds (blowing from North America to the Pacific) that act to interrupt the typical El Niño pattern characterized by flow from the Pacific to North America. In contrast, the largest biases in February (Fig. 9f) are found over the northeastern tip of Siberia, with considerably less bias over the northeast Pacific and west coast. We believe that it is these differences in the characteristic features of the January and February biases that lead to substantial errors in El Niño response over the northeast Pacific in January, whereas this is much less so in February.

The higher prediction skill over North America during February appears to be due to two different factors. First, predictions of the circulation anomaly in the northeast Pacific need not be particularly accurate in phase, since it is only necessary to place the anomaly far enough off the coast so that it does not produce erroneous precipitation along the west coast, something the GEOS model seems to be predisposed to do. Second, the model must produce an enhanced jet along the southern tier of states associated with a negative height anomaly over much of the southern United States, producing enhanced precipitation in the southern tier of states and the southeast. The model seems to be able to reproduce those anomalies reasonably well. Why that should be is unclear, although our SWM results indicate that that circulation anomaly (a negative streamfunction anomaly produced by the SWM in that region) is a robust response to the heating in the central-eastern tropical Pacific (e.g., Fig. 6).

While we believe these findings (focused on the GEOS model) are general enough to be applicable to many other models, that can of course only be confirmed by carrying out similar analyses with those models. Additional studies are also needed to determine whether basically the same factors (phase errors in the relevant circulation anomalies) play an important role in determining the within-season monthly skill of T2m predictions, as well as whether similar factors hold for predictions made during La Niña events.

Acknowledgments. This study was funded by a grant from NASA's Modeling Analysis and Prediction program (NA14OAR4310221 and WBS 802678.02.17.01.33). The various model simulations and predictions used in this study were either carried out or facilitated by the NASA/GMAO subseasonal to seasonal prediction group. The computing resources for this work were provided by the NASA High-End Computing (HEC) Program through the NASA Center for Climate Simulation (NCCS) at GSFC.

REFERENCES

Adler, R. F., and Coauthors, 2003: The version 2 Global Precipitation Climatology Project (GPCP) monthly precipitation analysis (1979–present). *J. Hydrometeor.*, **4**, 1147–1167, https://doi.org/10.1175/1525-7541(2003)004<1147:TVGPCP>2.0.CO;2.

Bacmeister, J. T., and G. L. Stephens, 2011: Spatial statistics of likely convective clouds in CloudSat data. *J. Geophys. Res.*, **116**, D04104, https://doi.org/10.1029/2010JD014444.

——, M. J. Suarez, and F. R. Robertson, 2006: Rain reevaporation, boundary layer–convection interactions, and Pacific rainfall patterns in an AGCM. *J. Atmos. Sci.*, **63**, 3383–3403, https://doi.org/10.1175/JAS3791.1.

Barahona, D., A. M. Molod, J. Bacmeister, A. Nenes, A. Gettelman, H. Morrison, V. Phillips, and A. Eichmann, 2014: Development of two-moment cloud microphysics for liquid and ice within the NASA Goddard Earth Observing System Model (GEOS-5). *Geosci. Model Dev.*, **7**, 1733–1766, https://doi.org/10.5194/gmd-7-1733-2014.

Barnston, A. G., R. E. Livezey, and M. S. Halpert, 1991: Modulation of Southern Oscillation–Northern Hemisphere mid-winter climate relationships by the QBO. *J. Climate*, **4**, 203–217, https://doi.org/10.1175/1520-0442(1991)004<0203:MOSONH>2.0.CO;2.

Becker, E., H. van den Dool, and Q. Zhang, 2014: Predictability and forecast skill in NMME. *J. Climate*, **27**, 5891–5906, https://doi.org/10.1175/JCLI-D-13-00597.1.

Borovikov, A., R. Cullather, R. Kovach, J. Marshak, G. Vernieres, Y. Vikhliaev, B. Zhao, and Z. Li, 2019: GEOS-5 seasonal forecast system. *Climate Dyn.*, **53**, 7335–7361, https://doi.org/10.1007/s00382-017-3835-2.

Chen, L.-C., H. van den Dool, E. Becker, and Q. Zhang, 2017: ENSO precipitation and temperature forecasts in the North American Multimodel Ensemble: Composite analysis and validation. *J. Climate*, **30**, 1103–1125, https://doi.org/10.1175/JCLI-D-15-0903.1.

Chen, M., P. Xie, J. E. Janowiak, and P. A. Arkin, 2002: Global land precipitation: A 50-yr monthly analysis based on gauge observations. *J. Hydrometeor.*, **3**, 249–266, https://doi.org/10.1175/1525-7541(2002)003<0249:GLPAYM>2.0.CO;2.

Colarco, P., A. DaSilva, M. Chin, and T. Diehl, 2010: Online simulations of global aerosol distributions in the NASA GEOS-4 model and comparisons to satellite and ground-based aerosol optical depth. *J. Geophys. Res.*, **115**, D14207, https://doi.org/10.1029/2009JD012820.

Collow, A. B. M., S. P. Mahanama, M. G. Bosilovich, R. D. Koster, and S. D. Schubert, 2017: An evaluation of teleconnections over the United States in an ensemble of AMIP simulations with the MERRA-2 configuration of the GEOS atmospheric model. Tech. Rep. NASA/TM-2017-104606, 68 pp.

Cullather, R. I., S. M. Nowicki, B. Zhao, and M. J. Suarez, 2014: Evaluation of the surface representation of the Greenland ice sheet in a general circulation model. *J. Climate*, **27**, 4835–4856, https://doi.org/10.1175/JCLI-D-13-00635.1.

Dawson, A., A. J. Matthew, and D. P. Stevens, 2011: Rossby wave dynamics of the North Pacific extra-tropical response to El Niño: Importance of the basic state in coupled GCMs. *Climate Dyn.*, **37**, 391–405, https://doi.org/10.1007/s00382-010-0854-7.

Ely, L. L., Y. Enzel, and D. R. Cayan, 1994: Anomalous North Pacific atmospheric circulation and large winter floods in the southwestern United States. *J. Climate*, **7**, 977–987, https://doi.org/10.1175/1520-0442(1994)007<0977:ANPACA>2.0.CO;2.

Gates, W. L., 1992: AMIP: The Atmospheric Model Intercomparison Project. *Bull. Amer. Meteor. Soc.*, **73**, 1962–1970, https://doi.org/10.1175/1520-0477(1992)073<1962:ATAMIP>2.0.CO;2.

Gelaro, R., and Coauthors, 2017: The Modern-Era Retrospective Analysis for Research and Applications, version 2 (MERRA-2). *J. Climate*, **30**, 5419–5454, https://doi.org/10.1175/JCLI-D-16-0758.1.

Gershunov, A., and T. Barnett, 1998: ENSO influence on intraseasonal extreme rainfall and temperature frequencies in the contiguous United States: Observations and model results. *J. Climate*, **11**, 1575–1586, https://doi.org/10.1175/1520-0442(1998)011<1575:EIOIER>2.0.CO;2.

GMAO, 2019a: MERRA-2 tavgM_2d_slv_Nx: 2d, Monthly mean, time-averaged, single-level, assimilation, assimilated meteorological fields, version 5.12.4. Goddard Space Flight Center Distributed Active Archive Center (GSFC DAAC), accessed March 2019, https://doi.org/10.5067/AP1B0BA5PD2K.

——, 2019b: MERRA-2 tavgM_3d_tdt_Np: 3d, Monthly mean, time-averaged, pressure-level, assimilation, temperature tendencies, version 5.12.4. GSFC DAAC, accessed March 2019, https://doi.org/10.5067/VILT59HI2MOY.

Griffies, S. M., 2012: Elements of the Modular Ocean Model (MOM): 2012 release. GFDL Ocean Group Tech. Rep. 7, NOAA/Geophysical Fluid Dynamics Laboratory, Princeton, NJ, 618 pp., http://mom-ocean.org/web/docs/project/MOM5_elements.pdf.

Henderson, S. A., E. D. Maloney, and S.-W. Son, 2017: Madden–Julian Oscillation Pacific teleconnections: The impact of the basic state and MJO representation in general circulation models. *J. Climate*, **30**, 4567–4587, https://doi.org/10.1175/JCLI-D-16-0789.1.

Hoerling, M. P., A. Kumar, and M. Zhong, 1997: El Niño, La Niña, and the nonlinearity of their teleconnections. *J. Climate*, **10**, 1769–1786, https://doi.org/10.1175/1520-0442(1997)010<1769:ENOLNA>2.0.CO;2.

——, J. W. Hurrell, T. Xu, G. T. Bates, and A. Phillips, 2004: Twentieth century North Atlantic climate change. Part II: Understanding the effect of Indian Ocean warming. *Climate Dyn.*, **23**, 391–405, https://doi.org/10.1007/s00382-004-0433-x.

Horel, J. D., and J. M. Wallace, 1981: Planetary-scale atmospheric phenomena associated with the Southern Oscillation. *Mon. Wea. Rev.*, **109**, 813–829, https://doi.org/10.1175/1520-0493(1981)109<0813:PSAPAW>2.0.CO;2.

Hoskins, B. J., and D. Karoly, 1981: The steady linear response of a spherical atmosphere to thermal and orographic forcing. *J. Atmos. Sci.*, **38**, 1179–1196, https://doi.org/10.1175/1520-0469(1981)038<1179:TSLROA>2.0.CO;2.

Hunke, E. C., and W. H. Lipscomb, 2008: CICE: The Los Alamos Sea Ice Model. Documentation and software user's manual, version 4.0. Tech. Rep. LA-CC-06-012, T-3 Fluid Dynamics Group, Los Alamos National Laboratory, 72 pp.

Jin, F., and B. J. Hoskins, 1995: The direct response to tropical heating in a baroclinic atmosphere. *J. Atmos. Sci.*, **52**, 307–319, https://doi.org/10.1175/1520-0469(1995)052<0307:TDRTTH>2.0.CO;2.

Jong, B.-T., M. Ting, and R. Seager, 2016: El Niño's impact on California precipitation: Seasonality, regionality, and El Niño intensity. *Environ. Res. Lett.*, **11**, 054021, https://doi.org/10.1088/1748-9326/11/5/054021.

Joseph, R., and S. Nigam, 2006: ENSO evolution and teleconnections in IPCC's twentieth-century climate simulations: Realistic representation? *J. Climate*, **19**, 4360–4377, https://doi.org/10.1175/JCLI3846.1.

Kirtman, B., and Coauthors, 2014: The North American Multi-Model Ensemble (NMME): Phase-1 seasonal to interannual prediction; Phase-2 toward developing intra-seasonal prediction. *Bull. Amer. Meteor. Soc.*, **95**, 585–601, https://doi.org/10.1175/BAMS-D-12-00050.1.

Koster, R., M. J. Suarez, A. Ducharne, M. Stieglitz, and P. Kumar, 2000: A catchment-based approach to modeling land surface processes in a general circulation model: 1. Model structure. *J. Geophys. Res.*, **105**, 24 809–24 822, https://doi.org/10.1029/2000JD900327.

Kumar, A., M. Hoerling, M. Ji, A. Leetmaa, and P. Sardeshmukh, 1996: Assessing a GCM's suitability for making seasonal predictions. *J. Climate*, **9**, 115–129, https://doi.org/10.1175/1520-0442(1996)009<0115:AAGSFM>2.0.CO;2.

Lim, Y.-K., S. D. Schubert, O. Reale, M.-Y. Lee, A. M. Molod, and M. J. Suarez, 2015: Sensitivity of tropical cyclones to parameterized convection in the NASA GEOS-5 model. *J. Climate*, **28**, 551–573, https://doi.org/10.1175/JCLI-D-14-00104.1.

Lin, H., and Z. Wu, 2011: Contribution of the autumn Tibetan Plateau snow cover to seasonal prediction of North American winter temperature. *J. Climate*, **24**, 2801–2813, https://doi.org/10.1175/2010JCLI3889.1.

Liu, S., Q. Wu, X. Ren, and Y. Yao, 2017: Modeled Northern Hemisphere autumn and winter climate responses to realistic Tibetan Plateau and Mongolia snow anomalies. *J. Climate*, **30**, 9435–9454, https://doi.org/10.1175/JCLI-D-17-0117.1.

Mason, S. J., and L. Goddard, 2001: Probabilistic precipitation anomalies associated with ENSO. *Bull. Amer. Meteor. Soc.*, **82**, 619–638, https://doi.org/10.1175/1520-0477(2001)082<0619:PPAAWE>2.3.CO;2.

Meehl, G. A., and H. Teng, 2007: Multi-model changes in El Niño teleconnections over North America in a future warmer climate. *Climate Dyn.*, **29**, 779–790, https://doi.org/10.1007/s00382-007-0268-3.

Molod, A. M., L. Takacs, M. J. Suarez, and J. Bacmeister, 2015: Development of the GEOS-5 atmospheric general circulation model: Evolution from MERRA to MERRA2. *Geosci. Model Dev.*, **8**, 1339–1356, https://doi.org/10.5194/gmd-8-1339-2015.

——, and Coauthors, 2020: GEOS-S2S version 2: The GMAO high-resolution coupled model and assimilation system for seasonal prediction. *J. Geophys. Res. Atmos.*, **125**, e2019JD031767, https://doi.org/10.1029/2019JD031767.

Moorthi, S., and M. J. Suarez, 1992: Relaxed Arakawa-Schubert: A parameterization of moist convection for general circulation models. *Mon. Wea. Rev.*, **120**, 978–1002, https://doi.org/10.1175/1520-0493(1992)120<0978:RASAPO>2.0.CO;2.

Philander, S., 1983: El Niño Southern Oscillation phenomena. *Nature*, **302**, 295–301, https://doi.org/10.1038/302295a0.

Putman, W. M., and S.-J. Lin, 2007: Finite-volume transport on various cubed-sphere grids. *J. Comput. Phys.*, **227**, 55–78, https://doi.org/10.1016/j.jcp.2007.07.022.

Rasmusson, E. M., and J. M. Wallace, 1983: Meteorological aspects of the El Niño/Southern Oscillation. *Science*, **222**, 1195–1202, https://doi.org/10.1126/science.222.4629.1195.

Ropelewski, C. F., and M. S. Halpert, 1986: North American precipitation and temperature patterns associated with the El Niño/Southern Oscillation (ENSO). *Mon. Wea. Rev.*, **114**, 2352–2362, https://doi.org/10.1175/1520-0493(1986)114<2352:NAPATP>2.0.CO;2.

Schonher, T., and S. E. Nicholson, 1989: The relationship between California rainfall and ENSO events. *J. Climate*, **2**, 1258–1269, https://doi.org/10.1175/1520-0442(1989)002<1258:TRBCRA>2.0.CO;2.

Schubert, S. D., Y. Chang, M. J. Suarez, and P. J. Pegion, 2008: ENSO and wintertime extreme precipitation events over the contiguous United States. *J. Climate*, **21**, 22–39, https://doi.org/10.1175/2007JCLI1705.1.

Seager, R., N. Naik, M. Ting, M. A. Cane, N. Harnik, and Y. Kushnir, 2010: Adjustment of the atmospheric circulation to tropical Pacific SST anomalies: Variability of transient eddy propagation in the Pacific–North America sector. *Quart. J. Roy. Meteor. Soc.*, **136**, 277–296, https://doi.org/10.1002/qj.588.

Ting, M., and P. D. Sardeshmukh, 1993: Factors determining the extratropical response to equatorial diabatic heating anomalies. *J. Atmos. Sci.*, **50**, 907–918, https://doi.org/10.1175/1520-0469(1993)050<0907:FDTERT>2.0.CO;2.

——, and L. Yu, 1998: Steady response to tropical heating in wavy linear and nonlinear baroclinic models. *J. Atmos. Sci.*, **55**, 3565–3582, https://doi.org/10.1175/1520-0469(1998)055<3565:SRTTHI>2.0.CO;2.

Trenberth, K. E., G. W. Branstator, D. Karoly, A. Kumar, N. Lau, and C. Ropelewski, 1998: Progress during TOGA in understanding and modeling global teleconnections associated with tropical sea surface temperature. *J. Geophys. Res.*, **103**, 14 291–14 324, https://doi.org/10.1029/97JC01444.

Weare, B. C., 2013: El Niño teleconnections in CMIP5 models. *Climate Dyn.*, **41**, 2165–2177, https://doi.org/10.1007/s00382-012-1537-3.

Webster, P. J., 1981: Mechanisms determining the atmospheric response to sea surface temperature anomalies. *J. Atmos. Sci.*, **38**, 554–571, https://doi.org/10.1175/1520-0469(1981)038<0554:MDTART>2.0.CO;2.

Yang, X., and T. DelSole, 2012: Systematic comparison of ENSO teleconnection patterns between models and observations. *J. Climate*, **25**, 425–446, https://doi.org/10.1175/JCLI-D-11-00175.1.

Yasui, S., and M. Watanabe, 2010: Forcing processes of the summertime circumglobal teleconnection pattern in a dry AGCM. *J. Climate*, **23**, 2093–2114, https://doi.org/10.1175/2009JCLI3323.1.